

Probing the rotational spin-Hall effect in a structured Gaussian beam

Ram Nandan Kumar¹, Yatish¹, Subhasish Dutta Gupta,^{1,2,3} Nirmalya Ghosh,^{1,*} and Ayan Banerjee^{1,†}

¹*Department of Physical Sciences, Indian Institute of Science Education and Research, Kolkata, Mohanpur, West Bengal 741246, India*

²*School of Physics, Hyderabad Central University, Serilingampally, Telangana 500046, India*

³*Tata Institute of Fundamental Research, Hyderabad, Telangana 500046, India*



(Received 10 June 2021; accepted 12 January 2022; published 4 February 2022)

Spin-to-orbit conversion of light is a dynamical optical phenomenon in nonparaxial fields leading to various manifestations of the spin and orbital Hall effect. However, the effects of the spin-orbit interaction (SOI) have not been explored extensively for structured Gaussian beams carrying no intrinsic orbital angular momentum. Indeed, the SOI effects on such structured beams can be directly visualized due to azimuthal rotation of their transverse intensity profiles, a phenomenon we call the rotational spin-Hall effect. In this paper we show that for an input circularly polarized (right or left) Hermite-Gaussian (HG₁₀) mode, the SOI leads to a significant azimuthal rotation of the transverse intensity distribution of both the orthogonal circularly polarized (left or right) component and the longitudinal field intensity with respect to the input intensity profile. We validate our theoretical and numerically simulated results experimentally by tightly focusing a circularly polarized HG₁₀ beam in an optical tweezers configuration and projecting out the opposite circular polarization component and the transverse distribution of the longitudinal field intensity at the output of the tweezers. We also measure the rotational shift as a function of the refractive index contrast in the path of the tightly focused light and in general observe a proportional increase. The enhanced spin-orbit conversion in these cases may lead to interesting applications in inducing complex dynamics in optically trapped birefringent particles using structured Gaussian beams with no intrinsic orbital angular momentum.

DOI: [10.1103/PhysRevA.105.023503](https://doi.org/10.1103/PhysRevA.105.023503)

I. INTRODUCTION

Spin angular momentum (SAM) and orbital angular momentum (OAM) are nearly independent quantities when light beams propagate paraxially in vacuum or through isotropic and homogeneous media [1–3]. However, propagation through inhomogeneous or anisotropic media [4], scattering processes [5], and tight focusing in isotropic inhomogeneous media lead to interactions between SAM and OAM, giving rise to tangible effects in the mesoscopic scale with applications in nanosensing [5], or particle manipulation [6]. In the case of tight focusing in optical tweezers, even a fundamental Gaussian beam evolves nonparaxially due to the presence of a spin-orbit and an orbit-orbit interaction term in the expression of total angular momentum so that $J = S(\sigma) + L_1(l) + L_2(\sigma + l)$ [5,7–10], where L_2 is the spin-orbit interaction (SOI) term. Now both the spin-orbit interaction term and the orbit-orbit interaction terms are enhanced as a result of the generation of a large longitudinal component of the electric field due to tight focusing and further accentuated by inserting a refractive index contrast in the path of the light beam that increases the geometric phase gradient of the focused light. Another interesting manifestation of the interplay between spin and orbital angular momenta arises

in the spin and orbital Hall effect, which is essentially the transverse spatial separation of opposite angular momentum components induced by the spin-orbit and orbit-orbit interactions, preserving the angular momentum conservation law. This angular-momentum-dependent separation may be represented in terms of spin-spin separation called the spin-Hall effect [8,11–16], orbit-orbit separation called the orbital Hall effect [17–19], and spin-orbit separation called the spin-orbit Hall effect [20], where the transverse spatial separation of the respective opposite spin and/or orbital angular momentum components is observed.

The spin and orbital Hall effects have been extensively studied in both fundamental Gaussian beams [6] and orbital angular momentum carrying Laguerre-Gaussian (LG) beams [1,21], with interesting effects in spin-orbit and orbit-orbit conversions in tightly focused LG beams leading to intriguing orbital motion of single optically trapped birefringent particles [22]. However, the effects of the spin-orbit interaction in structured Gaussian beams carrying no intrinsic orbital angular momentum [typically called Hermite-Gaussian (HG) beams] have largely been ignored in the literature. A study of such beams, however, merits attention, since any HG mode may be written as a superposition of two LG modes having opposite topological charge. This may lead to very interesting effects of the spin-orbit interaction, especially in the case of input spin-polarized HG beams. In addition, the breaking of azimuthal symmetry in the intensity profile distribution of such beams may lead to direct visualization of SOI effects in the beam structure itself.

*nghosh@iiserkol.ac.in

†ayan@iiserkol.ac.in

In this paper we study this problem in detail and demonstrate clear manifestations of azimuthal rotation of the transverse intensity profile of a circularly polarized HG₁₀ beam after it is tightly focused using optical tweezers. We describe this as a rotational spin-Hall effect. Interestingly, while rotation of the intensity profile due to spin-orbit conversion has been experimentally observed in speckle patterns emanating from multimode optical fibers (the optical Magnus effect) [23,24], it has not been observed for light beams, since most Gaussian beams (both fundamental and angular momentum carrying) possess circular symmetry in their transverse profiles, rendering the observation of such rotations impossible. The HG_{*nm*} modes, by virtue of their rectangular symmetry, actually provide excellent avenues for observing such rotations. Thus, we observe that for an input right-circularly polarized (RCP) or left-circularly polarized (LCP) HG₁₀ mode, tight focusing using a high numerical aperture (NA) objective lens in an optical tweezers setup leads to the generation of the opposite spin component that is also coupled with a corresponding orbital angular momentum mode, with the final effect being the rotation of the transverse intensity profile of the output. For the same reason, the transverse distribution of the longitudinal field component generated due to nonparaxial

propagation of the light [25–29] also displays a rotation. The magnitude of rotation for the respective components is determined by the diffraction integrals (or Debye-Wolf integrals) I_{11} , I_{12} , and I_{14} for transverse field components and I_{10} and I_{13} for longitudinal field components, which provide the extent of the spin-to-orbit conversion of angular momentum [5,30]. We also study the dependence of the rotation on the refractive index (RI) contrast in the path of the beam after it is tightly focused and observe that the rotational spin-Hall effect in general increases monotonically with increasing RI contrast. We verify this experimentally by projecting out the opposite spin-polarized transverse intensity component from the input and the longitudinal component in an optical tweezers configuration.

II. THEORY

We employ the Debye-Wolf theory or angular spectrum method [30,31] to determine the electric field at the output of the high NA objective lens for an input spin-polarized HG beam, also considering RI stratification of the media through which the beam travels after focusing [6,30–33]. The expression of the output electric field from the input electric field may be written as

$$\begin{bmatrix} E_x^o \\ E_y^o \\ E_z^o \end{bmatrix} = \begin{bmatrix} iI_{11} \cos \psi + iI_{14} \cos 3\psi & -iI_{12} \sin \psi + iI_{14} \sin 3\psi & 2I_{10} - 2I_{13} \cos 2\psi \\ -iI_{12} \sin \psi + iI_{14} \sin 3\psi & i(I_{11} + 2I_{12}) \cos \psi - iI_{14} \cos 3\psi & -2I_{13} \sin 2\psi \\ -2I_{10} + 2I_{13} \cos 2\psi & 2I_{13} \sin 2\psi & i(I_{11} - I_{12}) \cos \psi \end{bmatrix} \times \begin{bmatrix} E_x^i \\ E_y^i \\ E_z^i \end{bmatrix}. \quad (1)$$

Here \vec{E}^o and \vec{E}^i denote the output and input electric fields related through the 3×3 Jones matrix, respectively; I_{10} , I_{11} , I_{12} , I_{14} , and I_{13} are the Debye-Wolf integrals; and ψ is the azimuthal angle in the cylindrical (or spherical) coordinate system. Now, given that the Jones vectors for x - and y -polarized input light are $\mathbf{E}_x^i = [1 \ 0 \ 0]^\top$ and $\mathbf{E}_y^i = [0 \ 1 \ 0]^\top$, from Eq. (1) the output electric field for HG₁₀ input x -polarized light is given by

$$\begin{bmatrix} E_x^o \\ E_y^o \\ E_z^o \end{bmatrix}_{x\text{-pol}} = \begin{bmatrix} iI_{11} \cos \psi + iI_{14} \cos 3\psi \\ -iI_{12} \sin \psi + iI_{14} \sin 3\psi \\ -2I_{10} + 2I_{13} \cos 2\psi \end{bmatrix}. \quad (2)$$

It is important to note that a circularly polarized HG₁₀ beam does not carry OAM, but does possess an SAM of magnitude $\pm\hbar$, so the total angular momentum equals the SAM. Now, noting that the Jones vectors for input RCP and LCP light are $\mathbf{E}_{\text{RCP,LCP}} = [1 \ \pm i \ 0]^\top$, we use Eq. (1) to determine the output electric field in both cases as $[E_x^o E_y^o E_z^o]_{\text{RCP,LCP}}^\top = [a \ b \ c]^\top$, where $a = iI_{11} \cos \psi \pm I_{12} \sin \psi + I_{14}(i \cos 3\psi \mp \sin 3\psi)$, $b = -iI_{12} \sin \psi + iI_{14} \sin 3\psi \mp (I_{11} + 2I_{12}) \cos \psi \pm I_{14} \cos 3\psi$, and $c = -2I_{10} + 2I_{13} \cos 2\psi \pm 2iI_{13} \sin 2\psi$.

We then decompose the above output electric fields for input RCP or LCP light in terms of the SAM and OAM components (note that the effects of SOI cause all helicity components to be present along with the corresponding OAM

modes in the output electric field)

$$\begin{bmatrix} E_x^o \\ E_y^o \\ E_z^o \end{bmatrix}_{\text{RCP,LCP}} = \frac{i}{2} (I_{11} e^{\pm i\psi} + I_{11} e^{\mp i\psi} + I_{12} e^{\pm i\psi} + I_{12} e^{\mp i\psi}) \times \begin{bmatrix} 1 \\ \pm i \\ 0 \end{bmatrix} + i(I_{14} e^{\pm 3i\psi} - I_{12} e^{\pm i\psi}) \begin{bmatrix} 1 \\ \mp i \\ 0 \end{bmatrix} + (2I_{13} e^{\pm 2i\psi} - 2I_{10}) \begin{bmatrix} 0 \\ 0 \\ 1 \end{bmatrix}. \quad (3)$$

It is clear that the first four terms are associated with the same helicity as the input light, coupled correspondingly with appropriate positive and negative OAMs, respectively. The fifth and sixth terms appear purely due to SOI and thus denote opposite helicity with $l = \pm\hbar$ and $l = \pm 3\hbar$, respectively, satisfying the conservation of total angular momentum. The longitudinal component of the field with $l = \pm 2\hbar$ and $l = 0$ appears in the last two terms. Understandably, the effects of SOI would be extracted by projecting out the field components having the opposite helicity to the input field, as well as the longitudinal component. The intensity corresponding to these terms is obtained from Eq. (3) as $I_{\text{SOI}}(\rho, \psi) = I_{\text{trans}} + I_{\text{long}}$, where the transverse intensity component is given by

$$I_{\text{trans}} = 2(|I_{12}|^2 + |I_{14}|^2) - 2(I_{12}I_{14}^* + I_{14}I_{12}^*) \cos 2\psi + 2i(I_{12}I_{14}^* - I_{14}I_{12}^*) \sin 2\psi \quad (4)$$

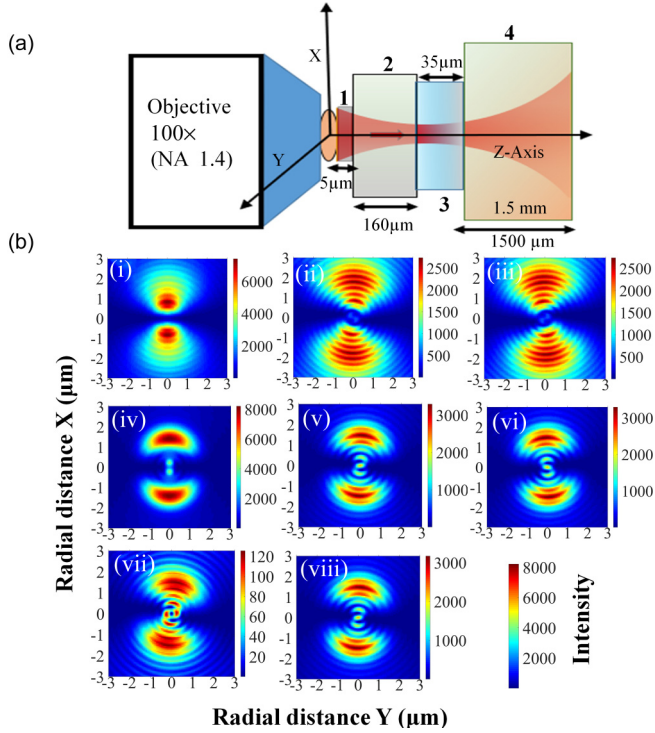


FIG. 1. (a) Schematic of the stratified medium used in our numerical simulation. (b) Simulation of the rotation of I_{SOI} at $z = 2 \mu\text{m}$ away the focus of the high NA objective (trap focus) for an input HG_{10} beam mode for (i)–(iii) matched RI and (iv)–(vi) mismatched RI 1.814 for (i) and (iv) input x -polarized light, (ii) and (v) input RCP, (iii) and (vi) input LCP light, (vii) rotation due to transverse components for RI 1.814, and (viii) rotation due to transverse distribution of longitudinal intensity profile for input RCP using RI 1.814.

and the longitudinal component is given by

$$I_{\text{long}} = 4(|I_{10}|^2 + |I_{13}|^2) - 4(I_{10}I_{13}^* + I_{13}I_{10}^*) \cos 2\psi \\ \pm 4i(I_{10}I_{13}^* - I_{13}I_{10}^*) \sin 2\psi. \quad (5)$$

Now, for an input RCP (LCP) HG_{10} mode, both I_{trans} and I_{long} display an azimuthal rotation about the input beam axis in a clockwise (counterclockwise) direction [Fig. 1(b)]. We observe these effects in our numerical simulations that we describe next.

III. NUMERICAL SIMULATIONS

As shown in Fig. 1(a), the laser beam of wavelength 671 nm is incident on the 100 \times oil-immersion objective of NA 1.4 followed by a stratified medium consisting of (1) an oil layer of thickness around 5 μm and RI 1.516, (2) a 160- μm -thick coverslip having refractive indices 1.516, 1.572, 1.695, and 1.814 (note that the case where the RI equals 1.516 is henceforth referred to as the matched condition, which is typically employed in optical tweezers to minimize spherical aberration effects in the focused beam spot), (3) a water layer (chosen since probe particles in future experiments will be immersed in water) having a refractive index of 1.33 with a depth of 35 μm , and finally (4) a glass slide of refractive index 1.516 whose thickness we consider to be semi-infinite ($\sim 1500 \mu\text{m}$). In the simulation, the origin of the coordinates is

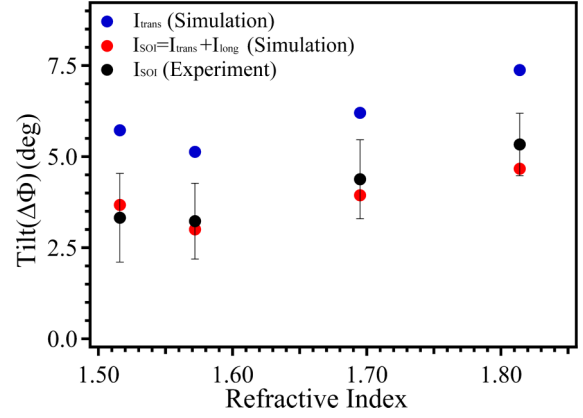


FIG. 2. Measurement of the rotational spin-Hall effect for simulated I_{trans} (blue circles), simulated $I_{SOI} = I_{\text{trans}} + I_{\text{long}}$ (red circles), and experimentally measured I_{SOI} (black circles) as a function of RI of the coverslip.

taken inside the water layer at an axial distance of 5 μm from the interface between the water and the coverslip. Thus, the objective-oil interface is at $-170 \mu\text{m}$, the oil-coverslip interface is at $-5 \mu\text{m}$, the coverslip-sample chamber interface is at 30 μm .

In Fig. 1(b) we plot I_{SOI} [Figs. 1(b i)–1(b vi)] as well as I_{trans} [Fig. 1(b vii)] and I_{long} [Fig. 1(b viii)] separately $z = 2 \mu\text{m}$ away from the beam focus for both the matched RI for the coverslip [Figs. 1(b i)–1(b iii)] and a mismatched RI of 1.814 [Figs. 1(b iv)–1(b vi)]. Clearly, the intensity profiles appear rotated relative to the axis of the input modal distribution (rotational spin-Hall shift) in several cases. However, the rotation vanishes for input linear polarization [Figs. 1(b i) and 1(b iv)], since the shifts for the constituent RCP and LCP components cancel out. However, they are significantly high for both RCP [Figs. 1(b ii) and 1(b v)] and LCP [Figs. 1(b iii) and 1(b vi)] components. Note that the nonparaxial propagation of light also leads to a transverse distribution of the longitudinal field intensity that also displays a rotation. We compare the rotational effects of the different field intensity components in Figs. 1(b vii) and 1(b viii), where Fig. 1(b vii) shows the spin rotational shift due to only I_{trans} and Fig. 1(b viii) shows the transverse distribution of I_{long} and Fig. 1(b v) I_{SOI} , all for input RCP light. We measure the rotations with respect to the axis of the linearly polarized beam mode that does not undergo rotation after focusing and display the measured angles of rotation for an input RCP HG_{10} beam as a function of RI from simulations in Fig. 2. For an RI of 1.814, we observe a maximum of 7.4 $^\circ$ azimuthal rotation for I_{trans} , 4.5 $^\circ$ for the transverse distribution of I_{long} , and 4.7 $^\circ$ for I_{SOI} . Note here that the presence of fringelike features in Figs. 1(b ii), 1(b iii), and 1(b v)–1(b viii) are due to oscillations in the Bessel functions involved in both components of I_{SOI} [34] for input circular polarization. They are almost entirely absent for the total intensity term [Fig. 1(b i)] and that associated with input linear polarization [Fig. 1(b iv)]. They are observed with very small magnitude in the output intensity components with the same circular polarization as the input [see Fig. 6(a) in Appendix C], but are possibly of opposite phase with I_{long} , so they cancel

out when we take a sum of the two [see Figs. 6(c) and 6(d) of Appendix C].

We observe that an increase in RI contrast tends to increase the observed azimuthal rotation. This can be understood from the fact that both the geometric phase acquired by the circularly polarized light during propagation and its gradient are enhanced with increasing RI contrast. Importantly, it is the geometric phase that is responsible for the SOI during tight focusing. This is because the k vectors evolve adiabatically as the waves approach the focus, thus leading to a spin-redirection Berry phase. The gradient of this Berry phase creates an intrinsic OAM [35], which eventually causes the SOI and is at the heart of the observed spin-dependent azimuthal rotation of the intensity profile [34]. In addition, since the contribution of the transverse distribution of I_{long} is 90% or even more of I_{SOI} (see Fig. 5 of Appendix B), it is the rotation of this component that finally dominates in the transverse rotation of the I_{SOI} profile, which we finally measure experimentally. We now proceed to describe the experiments we performed to verify these simulations.

IV. EXPERIMENTS

A schematic of our experimental system is provided in Fig. 3(a). The optical tweezers is developed around an inverted microscope that uses a 100X NA 1.4 oil-immersion objective lens to tightly focus the input beam into the stratified medium described in Fig. 1(a). Thus, we dropcast around 20 μl of water (RI 1.33) into a sample chamber developed using a coverslip (RIs of 1.516, 1.572, 1.695, and 1.814, employed one at a time) and a glass slide (RI 1.516), so the water layer thickness is around 35 μm . We generate first-order LG beams by coupling a linear polarized Gaussian beam into a vortex half-wave retarder of zeroth order (q plate) which generates both radial and azimuthal polarized vector beams at mutually perpendicular orientations. Afterward, we use a linear polarizer to convert the radial (azimuthal) beams into HG_{10} (HG_{01}) modes. We pass the output beam from the linear polarizer through a quarter waveplate (QWP) centered at 671 nm and oriented at 45° to the input beam axis in order to circularly polarize the HG_{10} mode.

For imaging the focused beam in the far field, we collect the backscattered light from the sample chamber using the objective lens itself and pass it through another QWP in order to project out the intensity of the spin state we would like to detect. Thus, for incident RCP light, the output QWP filters out the RCP component, so we detect the intensity only of the LCP component superposed with the longitudinal component (I_{SOI}) on a CCD that we use to image the intensity profile. Note that, contrary to what we observed in the simulations, we do not observe weak interference fringes in our experiments, possibly due to the presence of an unpolarized component in the input beam which lowers the contrast of the fringes considerably. Now the tight focusing of a linearly polarized HG beam does not show any rotation of the axis of HG_{10} mode, which we verify first. In order to measure rotation of the output mode for input circularly polarized HG_{10} modes, we perform the experiments first with linear polarized light that display no rotation and can thus be employed as a reference to measure the rotation for input spin-polarized states. To

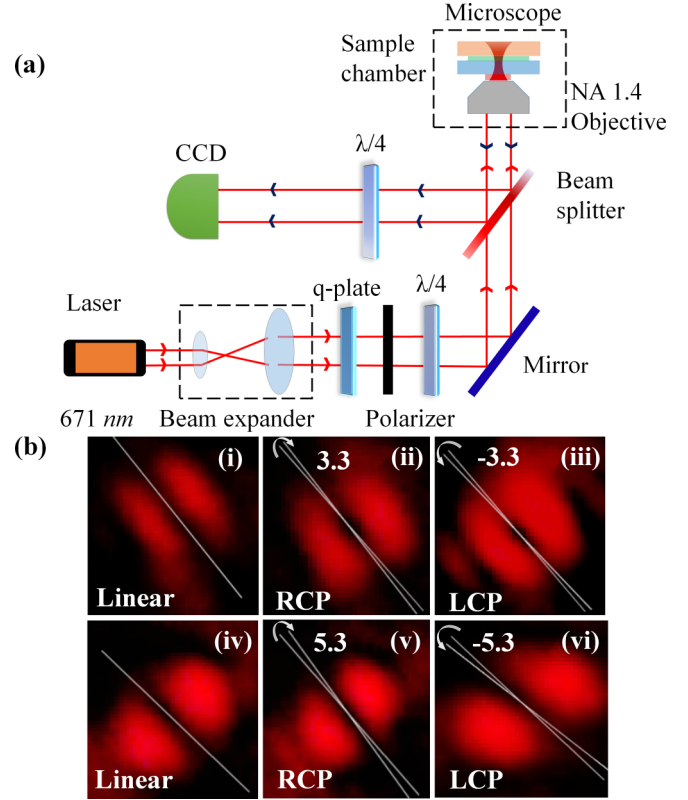


FIG. 3. (a) Schematic diagram of our experimental setup. (b) Experimental measurements of the rotational spin-Hall shift for RI matched and mismatched coverslips. Red arrows depict the beam coupled into the optical tweezers microscope, while the blue arrows depict the backscattered light used for imaging the output mode. Matched conditions for RI 1.516 are shown with (i) the CCD image of the output intensity profile for the input linearly polarized state which we use as a reference to measure rotations for input spin-polarized states, (ii) the output intensity profile for input RCP light, and (iii) the output intensity profile for input LCP light. Also shown are matched conditions for RI 1.814 with (iv) the reference linearly polarized input state, (v) the output intensity profile for input RCP, and (vi) the output intensity profile for input LCP. The white straight lines through the beam axes show the linear fit for the lowest-intensity pixels along the beam axis, which we determine from a least-squares fit in MATLAB.

determine the angle of rotation, we use the CCD image of the mode to determine the (x, y) coordinates and red, green, and blue (RGB) values of each pixel in the region around the axis of singularity [see the dark region in Fig. 3(b)] of the beam mode. We then proceed to select out the coordinates of the pixels with the lowest RGB values and fit a straight line to those pixels. We fit a straight line to the selected coordinates and determine the slope of the fit along with its standard deviation, which essentially provides the mean position of the zero line of the focused HG beam as well as its root-mean-square deviation. We perform this analysis for all output modes for the input linear and spin-polarized states and measure the angle of rotation of the axis from the slope with respect to the vertical axis. We display the results of the rotation of the beam axes in Figs. 3(b i)–3(b vi). Figures 3(b i)–3(b iii) display the rotational spin-Hall shift for the matched RI of

1.516, whereas Figs. 3(b iv)–3(b vi) are for an RI of 1.814. Also, Figs. 3(b i) and 3(b iv) represent the reference linear polarization states with respect to which we measure the rotational spin-Hall effect for the matched condition [input RCP and LCP light in Figs. 3(b ii) and 3(b iii), respectively] and RI of 1.814 [input RCP and LCP light in Figs. 3(b v) and 3(b vi), respectively]. Clearly, in the RCP and LCP cases, the zero line appears to be tilted in opposite directions with respect to the linearly polarized case, with the tilt higher for the mismatched condition. The actual measured values of rotation are shown in Fig. 2 (black circles) and we obtain a very good match with the values obtained from simulation (red circles). The errors in determining the rotation angles are between 5% and 20% for individual cases.

V. CONCLUSION

We have studied the rotational spin-Hall effect in a structured Gaussian beam (HG₀₁ mode) carrying no intrinsic OAM, when it is tightly focused through a high NA objective lens in an optical tweezers configuration with a stratified medium in the path of the focused light. For input circularly polarized states, the SOI effects due to tight focusing cause the generation of opposite circular polarization coupled with a corresponding OAM state to satisfy conservation of the total angular momentum. As a result, the intensity profile corresponding to these states undergoes a rotation with respect to the profile corresponding to the linearly polarized input state, allowing us to visualize the effects of the SOI in the output intensity profile itself. In addition, the transverse distribution of the longitudinal field intensity profile also undergoes a rotation due to coupling with OAM states due to the SOI. We quantified such rotations using the complete vector diffraction theory described by Debye and Wolf by numerical simulations of the output electric field after tight focusing through a stratified medium and verified our simulations via careful experiments, where we projected out the opposite circular polarization state along with the longitudinal component for a given input circular polarization. We obtained excellent matches with simulation and thus clearly demonstrated an interesting manifestation of the SOI for asymmetric (Hermite-Gaussian) modes of light. The rotational spin-Hall shift increases with RI contrast of the stratified medium, which was expected since the magnitude of the SOI increases correspondingly due to the enhanced geometric phase gradient in these cases. We would also like to point out that, while these studies were carried out on the spatial intensity profiles of a simple structured beam in an optical tweezers configuration, we would like to extend our study to higher-order structured beams where the SOI effects due to tight focusing would be much more intriguing. Experiments on the observation of rotation of optically trapped birefringent particles around the beam axis due to the generation of OAM by the SOI in such beams would thus lead to interesting routes of complex particle manipulation using optical tweezers.

ACKNOWLEDGMENTS

The authors acknowledge SERB, Department of Science and Technology, Government of India (Project No.

EMR/2017/001456) and IISER Kolkata IPh.D fellowship for financial support. They also acknowledge Anand Dev Ranjan and Sauvik Roy for their help with experiments and simulation.

APPENDIX A: THEORETICAL CALCULATIONS

The angular spectrum for the focal field can be expressed as a function of the field at the focus as [30]

$$\vec{E}(\rho, \psi, z) = i \frac{k f e^{-ikf}}{2\pi} \int_0^{\theta_{\max}} \int_0^{2\pi} \vec{E}_{\text{res}}(\theta, \phi) e^{ikz \cos \theta} \times e^{ik\rho \sin \theta \cos(\phi - \psi)} \sin(\theta) d\theta d\phi, \quad (\text{A1})$$

where f is the focal length of the lens and θ_{\max} is because of the finite size of the aperture which is decided by the NA of the objective lens. Note that here we cannot use the paraxial approximation for calculating the electric field at the focal plane, because we are using a high NA objective lens (NA equal to 1.4) for tight focusing. Thus, we use the angular spectrum method, which entails the exact solutions for the nonparaxial regime to determine the nature of electric field distribution of Hermite-Gaussian modes propagating in a medium or across a stratified medium. This approach operates in the frequency domain, calculates the Fourier transform (FT) of the input field, and multiplies the result with a transfer function so that the desired output field is obtained by the inverse FT. The transfer function is given by $A = R_z(\phi) T R_y(\theta) R_z(-\phi)$, where R_z and R_y are SO(3) rotation matrices [33]. Since the stratification of any medium makes the field propagating in the medium dependent on the input polarization, we incorporate the Fresnel transmission coefficients T_s and T_p as well as the Fresnel reflection coefficients R_s and R_p , considering the contributions from both the s and p polarization. The output and the incident field are related through a transfer function A as $\mathbf{E}_{\text{res}}(\theta, \phi) = A \mathbf{E}_{\text{inc}}(\theta, \phi)$, where the T and R matrices are given by

$$T = \begin{pmatrix} T_p & 0 & 0 \\ 0 & T_s & 0 \\ 0 & 0 & T_p \end{pmatrix}, \quad R = \begin{pmatrix} -R_p & 0 & 0 \\ 0 & R_s & 0 \\ 0 & 0 & -R_p \end{pmatrix}. \quad (\text{A2})$$

Note that we have $T_i^{(1,j)} = \frac{E_{i+}^j}{E_{i-}^j}$ and $R_i^{(1,j)} = \frac{E_{i-}^j}{E_{i+}^j}$. Here i specifies the polarization s and p , $+$ and $-$ signify a wave propagating forward and backward, respectively, and j in the superscript specifies the layer of the stratified medium in which the optical tweezers (trapping laser) focus lies. For an input HG₁₀ beam [30] we have

$$E_{\text{inc}}(\theta, \phi) = E_0 \left(\frac{2x_{\infty}}{w_0} \right) \exp \left\{ -\frac{x_{\infty}^2 + y_{\infty}^2}{w_0^2} \right\} \\ = \left(\frac{2E_0 f}{w_0} \right) \sin \theta \cos \phi e^{-f^2 \sin^2 \theta / w_0^2}.$$

From these equations we can write the output electric field from the input electric field in the form of a matrix equation as

$$\begin{bmatrix} E_x^o \\ E_y^o \\ E_z^o \end{bmatrix} = \begin{bmatrix} iI_{11} \cos \psi + iI_{14} \cos 3\psi & -iI_{12} \sin \psi + iI_{14} \sin 3\psi & 2I_{10} - 2I_{13} \cos 2\psi \\ -iI_{12} \sin \psi + iI_{14} \sin 3\psi & i(I_{11} + 2I_{12}) \cos \psi - iI_{14} \cos 3\psi & -2I_{13} \sin 2\psi \\ -2I_{10} + 2I_{13} \cos 2\psi & 2I_{13} \sin 2\psi & i(I_{11} - I_{12}) \cos \psi \end{bmatrix} \times \begin{bmatrix} E_x^i \\ E_y^i \\ E_z^i \end{bmatrix}, \quad (\text{A3})$$

where \mathbf{E}_o and \mathbf{E}_i denote the output and input Jones polarization vectors, respectively, and I_{10} , I_{11} , I_{12} , I_{14} , and I_{13} are the Debye-Wolf integrals for the transmitted and reflected waves, which are given as [31,32]

$$\begin{aligned} I'_{10}(\rho) &= \int_0^{\theta_{\max}} E_{\text{inc}}(\theta) \sqrt{\cos \theta} \sin^2 \theta T_p \sin \theta_j J_0(k_1 \rho \sin \theta) e^{ik_{jz} \cos \theta_j} d\theta, \\ I'_{11}(\rho) &= \int_0^{\theta_{\max}} E_{\text{inc}}(\theta) \sqrt{\cos \theta} \sin^2 \theta (T_s + 3T_p \cos \theta_j) J_1(k_1 \rho \sin \theta) e^{ik_{jz} \cos \theta_j} d\theta, \\ I'_{12}(\rho) &= \int_0^{\theta_{\max}} E_{\text{inc}}(\theta) \sqrt{\cos \theta} \sin^2 \theta (T_s - T_p \cos \theta_j) J_1(k_1 \rho \sin \theta) e^{ik_{jz} \cos \theta_j} d\theta, \\ I'_{13}(\rho) &= \int_0^{\theta_{\max}} E_{\text{inc}}(\theta) \sqrt{\cos \theta} \sin^2 \theta T_p \sin \theta_j J_2(k_1 \rho \sin \theta) e^{ik_{jz} \cos \theta_j} d\theta, \\ I'_{14}(\rho) &= \int_0^{\theta_{\max}} E_{\text{inc}}(\theta) \sqrt{\cos \theta} \sin^2 \theta (T_s - T_p \cos \theta_j) J_3(k_1 \rho \sin \theta) e^{ik_{jz} \cos \theta_j} d\theta, \\ I''_{11}(\rho) &= \int_0^{\theta_{\max}} E_{\text{inc}}(\theta) \sqrt{\cos \theta} \sin^2 \theta (R_s - 3R_p \cos \theta_j) J_1(k_1 \rho \sin \theta) e^{-ik_{jz} \cos \theta_j} d\theta, \\ I''_{12}(\rho) &= \int_0^{\theta_{\max}} E_{\text{inc}}(\theta) \sqrt{\cos \theta} \sin^2 \theta (R_s - R_p \cos \theta_j) J_1(k_1 \rho \sin \theta) e^{-ik_{jz} \cos \theta_j} d\theta, \\ I''_{13}(\rho) &= - \int_0^{\theta_{\max}} E_{\text{inc}}(\theta) \sqrt{\cos \theta} \sin^2 \theta R_p \sin \theta_j J_2(k_1 \rho \sin \theta) e^{-ik_{jz} \cos \theta_j} d\theta, \\ I''_{14}(\rho) &= \int_0^{\theta_{\max}} E_{\text{inc}}(\theta) \sqrt{\cos \theta} \sin^2 \theta (R_s + R_p \cos \theta_j) J_3(k_1 \rho \sin \theta) e^{-ik_{jz} \cos \theta_j} d\theta. \end{aligned}$$

Here the superscripts t and r denote the transmitted and reflected components, respectively, and J_n is the Bessel function of the first kind of order n .

The radial intensity distribution of the output electric field with an input RCP or LCP HG beam is given by

$$\begin{aligned} I_{\text{RCP,LCP}}(\rho, \psi) &= 2(|I_{12}|^2 + |I_{14}|^2) + 2(|I_{11}|^2 + |I_{12}|^2) \cos^2 \psi + 2(I_{11}I_{12}^* + I_{11}^*I_{12}) \cos^2 \psi \\ &\quad - 2(I_{12}I_{14}^* + I_{12}^*I_{14}) \cos 2\psi \pm 2i(I_{12}I_{14}^* - I_{12}^*I_{14}) \sin 2\psi. \end{aligned} \quad (\text{A4})$$

The equations for the intensity profile are different for input RCP and LCP HG₁₀ beams. Therefore, the rotation of the intensity profile for input RCP and LCP beams are in the clockwise and counterclockwise directions, respectively. The total intensity I_{SOI} profile is a linear combination of I_{trans} (orthogonal helicity components to the input helicity) and I_{long} of the HG₁₀ beam,

$$I_{\text{SOI}}(\rho, \psi) = I_{\text{trans}} + I_{\text{long}}. \quad (\text{A5})$$

The transverse intensity profile of orthogonal helicity components to the input helicity components of the HG₁₀ beam is

$$I_{\text{trans}}(\rho, \psi) = 2(|I_{12}|^2 + |I_{14}|^2) - 2(I_{12}I_{14}^* + I_{14}I_{12}^*) \cos 2\psi \pm 2i(I_{12}I_{14}^* - I_{14}I_{12}^*) \sin 2\psi.$$

The intensity due to longitudinal components of the RCP and LCP light of the HG₁₀ beam is

$$I_{\text{long}}(\rho, \psi) = 4(|I_{10}|^2 + |I_{13}|^2) - 4(I_{10}I_{13}^* + I_{13}I_{10}^*) \cos 2\psi \pm 4i(I_{10}I_{13}^* - I_{13}I_{10}^*) \sin 2\psi.$$

The intensity of the linearly polarized HG₁₀ beam is

$$\begin{aligned} I(\rho, \psi) &= |I_{14}|^2 + 4|I_{10}|^2 + |I_{11}|^2 \cos^2 \psi + |I_{12}|^2 \sin^2 \psi + 4|I_{13}|^2 \cos^2 2\psi \\ &\quad + \left(\frac{I_{11}I_{14}^*}{2} + \frac{I_{14}I_{11}^*}{2} - \frac{I_{12}I_{14}^*}{2} - \frac{I_{14}I_{12}^*}{2} - 4I_{10}I_{13}^* - 4I_{13}I_{10}^* \right) \cos 2\psi \\ &\quad + \left(\frac{I_{11}I_{14}^*}{2} + \frac{I_{14}I_{11}^*}{2} + \frac{I_{12}I_{14}^*}{2} + \frac{I_{14}I_{12}^*}{2} \right) \cos 4\psi. \end{aligned} \quad (\text{A6})$$

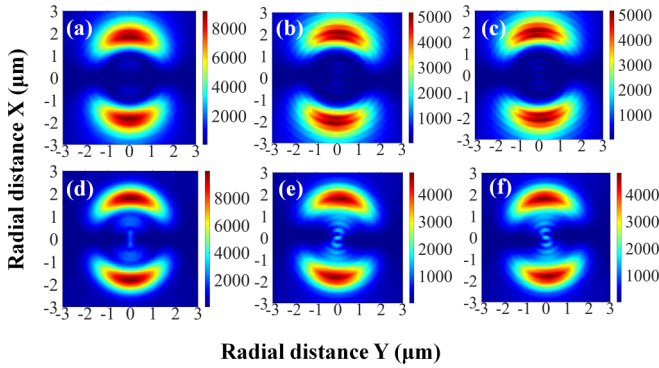


FIG. 4. Simulation of rotation of the total intensity profile $z = 2 \mu\text{m}$ away from the focus of the high NA objective (trap focus) for an input HG_{10} beam mode for mismatched RIs (a)–(c) 1.572 and (d)–(f) 1.695 for (a) and (d) input x -polarized light, (b) and (e) input RCP light, and (c) and (f) input LCP light.

APPENDIX B: NUMERICAL SIMULATIONS

We now run simulations on our experimental system (stratified medium in the path of the optical tweezers light beam) as described in the main text. According to Eq. (A5), the intensities corresponding to I_{SOI} of RCP and LCP components are different; therefore, the intensity profiles for the RCP and LCP input HG_{10} mode show clockwise and counterclockwise rotations with respect to the x axis in the transverse plane. We have provided results for the azimuthal rotation for RIs of 1.516 and 1.814 [Fig. 1(b)]; here we provide those for RIs of 1.572 and 1.659. Once again, we plot I_{SOI} as given in Eq. (A5). The simulation results are displayed in Figs. 4(a)–4(f). We also provide the values of rotation calculated from simulations and measured for experiments for all RI values in Table I. The measurement of the rotation angles are performed using the method described in the main text.

Another useful exercise is to compare the transverse distribution of the longitudinal intensity profile (I_{long}) to that of the transverse intensity component (I_{trans}) of the SOI-generated circular polarization that is opposite to the input polarization. This is displayed in Fig. 5. We observe that the field corresponding to I_{long} (normalized) dominates over the transverse component I_{trans} of the radial intensity (I_{SOI}), with the former being almost 90% of the sum of these two intensity components [refer to the I_{SOI} defined in the main text and in Fig. 1(b v)] in the radial direction. We also observe the contribution of the intensity profile of I_{long} to be increasing with increasing RI contrast of the stratified medium. However, when we consider the total intensity in the radial direction,

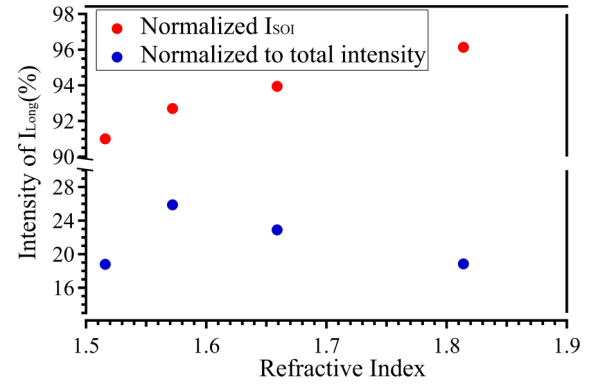


FIG. 5. Percentage of the longitudinal component of light compared to the spin-polarized transverse component induced by SOI (red circles) and total transverse intensity (blue circles).

which also contains the intensity for the circular polarization in the direction of the input polarization, the I_{long} field intensity is only 20%–30% of the total radial intensity. We also observe that this ratio reduces with increasing RI contrast, since the spread in the k vector is reduced correspondingly, resulting in a lower z component of the field compared to the total transverse component.

Finally, we comment on the fringelike structures visible in the intensity profiles of I_{SOI} , I_{trans} , and I_{long} , shown in Figs. 1(b ii), 1(b iii), and 1(b v)–1(b viii). These appear due to oscillations in the Bessel functions involved in both components of I_{SOI} for input circular polarization. They are almost entirely absent for the total intensity term [Fig. 1(b i)] and that associated with input linear polarization [Fig. 1(b iv)]. Also, they are observed with very small magnitude in the output intensity components with the same circular polarization as the input (RCP and RCP), which we observe in Fig. 6(a), as well as in the sum of the intensity profiles of the output RCP and LCP components [Fig. 6(b)]. However, the oscillations in the profile for the output RCP component is possibly of opposite phase to I_{long} , so they cancel out when we take a sum of the two [Fig. 6(c)], as well as for the total intensity [Fig. 6(d)]. Note that similar fringelike oscillations have been reported in Fig. 1(b) in [34] in a plot of terms containing Bessel functions different from J_0 .

APPENDIX C: EXPERIMENTS

We use a conventional optical tweezers configuration consisting of an inverted microscope (Carl Zeiss Axiovert.A1) with an oil-immersion $100\times$ objective (Zeiss, NA 1.4) and a He-Ne laser (Laserver, 671 nm, 200 mW) coupled into the back port

TABLE I. Values of rotation calculated from simulations and measured for experiments for all RI values.

RI	Simulation		Experiment	
	$\Delta\Phi$ (input RPC)	$\Delta\Phi$ (input LPC)	$\Delta\Phi$ (input RPC)	$\Delta\Phi$ (input LPC)
1.516	3.7	−3.7	3.3 ± 1.2	$−3.9 \pm 1.1$
1.572	3.0	−3.0	3.2 ± 1.0	$−3.1 \pm 1.3$
1.695	3.9	−3.9	4.4 ± 1.1	$−3.5 \pm 2.0$
1.814	4.7	−4.7	5.3 ± 0.9	$−5.2 \pm 1.5$

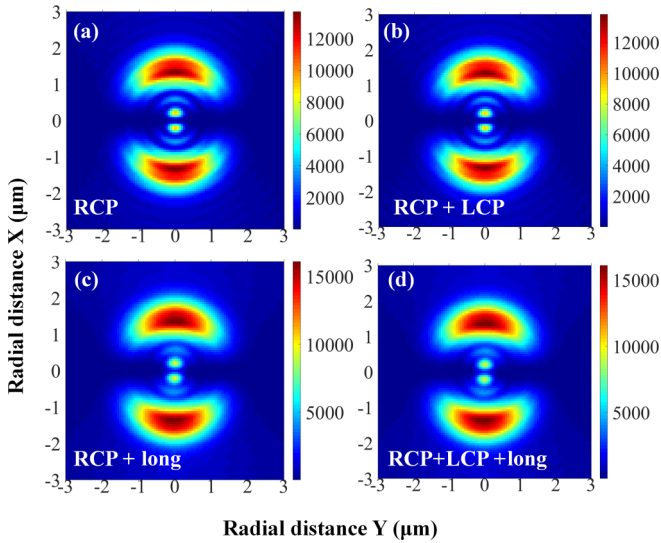


FIG. 6. Simulation of transverse intensity profile $z = 2 \mu\text{m}$ away from the focus of the high NA objective (trap focus) for an input RCP HG_{10} beam mode for mismatched RI 1.814 intensity due to (a) the RCP component of SOI, (b) the RCP and LCP components of SOI, (c) the RCP and longitudinal components of SOI, and (d) the RCP, LCP, and longitudinal components of SOI.

of the microscope. The sample chamber is prepared using a coverslip (RIs 1.516, 1.572, 1.695, and 1.814, employed one at a time) and a glass slide (RI 1.516), between which we dropcast around $20 \mu\text{l}$ of water (RI 1.33), so the water layer thickness is around $35 \mu\text{m}$. We generate first-order LG beams by coupling a linear polarized Gaussian beam into a vortex half-wave retarder of zeroth order (q plate, Thorlabs) which generates both radial and azimuthal polarized vector beams at different orientations, after which we use a linear polarizer to convert these into HG_{10} (HG_{01}) modes. We pass the output beam from the linear polarizer through a QWP centered at

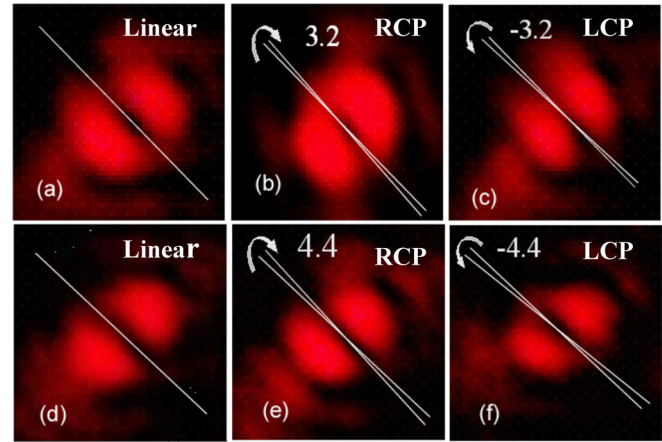


FIG. 7. Experimental measurements of the rotational spin-Hall shift for RI mismatched coverslips for (a)–(c) RI 1.572 with (a) the CCD image of the output intensity profile for the input linearly polarized state which we use as a reference to measure rotations for input spin-polarized states, (b) the output intensity profile for input RCP light, and (c) the output intensity profile for input LCP light and for (d)–(f) RI 1.695 with (d) the reference linearly polarized input state, (e) the output intensity profile for input RCP light, and (f) the output intensity profile for input LCP light. The white straight lines through the beam axes show the linear fit for the lowest-intensity pixels along the beam axis.

671 nm and oriented at 45° to the input beam axis in order to circularly polarize the HG_{10} mode.

Other than the experiments described in the main text, we have also performed experiments to determine the azimuthal rotation for an input RCP or LCP HG_{10} beam for RIs 1.572 and 1.695 of the coverslip in the stratified medium. The beam profiles are displayed in Figs. 7(a)–7(c) for RI 1.572 and 7(d)–7(f) for RI 1.695. The measured rotations agree well with the theoretically simulated values as shown in Fig. 2 and Table I.

- [1] A. T. O’Neil, I. MacVicar, L. Allen, and M. J. Padgett, *Phys. Rev. Lett.* **88**, 053601 (2002).
- [2] S. M. Barnett, L. Allen, R. P. Cameron, C. R. Gilson, M. J. Padgett, F. C. Speirits, and A. M. Yao, *J. Opt.* **18**, 064004 (2016).
- [3] L. Allen, M. W. Beijersbergen, R. J. C. Spreeuw, and J. P. Woerdman, *Phys. Rev. A* **45**, 8185 (1992).
- [4] Y. Zhao, J. S. Edgar, G. D. M. Jeffries, D. McGloin, and D. T. Chiu, *Phys. Rev. Lett.* **99**, 073901 (2007).
- [5] K. Y. Bliokh, F. J. Rodríguez-Fortuño, F. Nori, and A. V. Zayats, *Nat. Photon.* **9**, 796 (2015).
- [6] B. Roy, N. Ghosh, A. Banerjee, S. D. Gupta, and S. Roy, *New J. Phys.* **16**, 083037 (2014).
- [7] V. S. Liberman and B. Y. Zel’dovich, *Phys. Rev. A* **46**, 5199 (1992).
- [8] D. L. Andrews and M. Babiker, *The Angular Momentum of Light* (Cambridge University Press, Cambridge, 2012).
- [9] E. Hasman, G. Biener, A. Niv, and V. Kleiner, *Prog. Opt.* **47**, 215 (2005).
- [10] L. Marrucci, E. Karimi, S. Slussarenko, B. Piccirillo, E. Santamato, E. Nagali, and F. Sciarrino, *J. Opt.* **13**, 064001 (2011).
- [11] M. Onoda, S. Murakami, and N. Nagaosa, *Phys. Rev. Lett.* **93**, 083901 (2004).
- [12] C. Leyder, M. Romanelli, J. P. Karr, E. Giacobino, T. C. Liew, M. M. Glazov, A. V. Kavokin, G. Malpuech, and A. Bramati, *Nat. Phys.* **3**, 628 (2007).
- [13] O. Hosten and P. Kwiat, *Science* **319**, 787 (2008).
- [14] X. Yin, Z. Ye, J. Rho, Y. Wang, and X. Zhang, *Science* **339**, 1405 (2013).
- [15] Y. Qin, Y. Li, H. He, and Q. Gong, *Opt. Lett.* **34**, 2551 (2009).
- [16] X. Ling, X. Zhou, K. Huang, Y. Liu, C.-W. Qiu, H. Luo, and S. Wen, *Rep. Prog. Phys.* **80**, 066401 (2017).
- [17] K. Y. Bliokh, *Phys. Rev. Lett.* **97**, 043901 (2006).
- [18] M. Merano, N. Hermosa, J. P. Woerdman, and A. Aiello, *Phys. Rev. A* **82**, 023817 (2010).
- [19] Z. Zhang, Z. Xin-Xing, L. Xiao-Hui, C. Shi-Zhen, L. Hai-Lu, and W. Shuang-Chun, *Chin. Phys. B* **23**, 064215 (2014).
- [20] S. Fu, C. Guo, G. Liu, Y. Li, H. Yin, Z. Li, and Z. Chen, *Phys. Rev. Lett.* **123**, 243904 (2019).
- [21] Z. Bomzon and M. Gu, *Opt. Lett.* **32**, 3017 (2007).
- [22] Z. Shen, L. Su, X.-C. Yuan, and Y.-C. Shen, *Appl. Phys. Lett.* **109**, 241901 (2016).

- [23] A. V. Dooghin, N. D. Kundikova, V. S. Liberman, and B. Y. Zel'dovich, *Phys. Rev. A* **45**, 8204 (1992).
- [24] H. Luo, S. Wen, W. Shu, and D. Fan, *Phys. Rev. A* **81**, 053826 (2010).
- [25] N. Baranova, A. Y. Savchenko, and B. Y. Zel'dovich, *JETP Lett.* **59**, 232 (1994).
- [26] B. Y. Zel'dovich, N. Kundikova, and L. Rogacheva, *JETP Lett.* **59**, 737 (1994).
- [27] A. Bekshaev, *Ukr. J. Phys. Opt.* **12**, 10 (2011).
- [28] A. Y. Bekshaev, *J. Opt.* **19**, 085602 (2017).
- [29] A. Y. Bekshaev, *Phys. Rev. A* **85**, 023842 (2012).
- [30] L. Novotny and B. Hecht, *Principles of Nano-Optics* (Cambridge University Press, Cambridge, 2012).
- [31] B. Richards and E. Wolf, *Proc. R. Soc. London Ser. A* **253**, 358 (1959).
- [32] O. G. Rodríguez-Herrera, D. Lara, K. Y. Bliokh, E. A. Ostrovskaya, and C. Dainty, *Phys. Rev. Lett.* **104**, 253601 (2010).
- [33] A. Rohrbach, *Phys. Rev. Lett.* **95**, 168102 (2005).
- [34] B. Roy, N. Ghosh, S. D. Gupta, P. K. Panigrahi, S. Roy, and A. Banerjee, *Phys. Rev. A* **87**, 043823 (2013).
- [35] Z. Bomzon, M. Gu, and J. Shamir, *Appl. Phys. Lett.* **89**, 241104 (2006).